Full length article

Ultrafast synchrotron X-ray imaging studies of microstructure fragmentation in solidification under ultrasound

CrossMark

Bing Wang [a, b], Dongyue Tan [a], Tung Lik Lee [a, c], Jia Chuan Khong [a, d], Feng Wang [e], Dmitry Eskin [e], Thomas Connolley [f], Kamel Fezzaa [g], Jiawei Mi [a, *]

[a] School of Engineering & Computer Science, University of Hull, Hull, HU6 7RX, UK
[b] Department of Engineering, University of Cambridge, CB2 1PZ, UK
[c] ISIS Neutron Source, Rutherford Appleton Laboratory, Harwell Oxford, Didcot, OX11 0QX, UK
[d] Department of Medical Physics and Biomedical Engineering, University College London, London, WC1E 6BT, UK
[e] Brunel Centre for Advanced Solidification Technology, Brunel University London, Uxbridge, London, UB8 3PH, UK
[f] Diamond Light Source Ltd., Harwell Campus, Didcot, OX11 0DE, UK
[g] Advanced Photon Source, Argonne National Laboratory, Argonne, IL, 60439, USA

ARTICLE INFO

ABSTRACT

Ultrasound processing of metal alloys is an environmental friendly and promising green technology for liquid metal degassing and microstructural refinement. However many fundamental issues in this field are still not fully understood, because of the difficulties in direct observation of the dynamic behaviours caused by ultrasound inside liquid metal and semisolid metals during the solidification processes. In this paper, we report a systematic study using the ultrafast synchrotron X-ray imaging (up to 271,554 frame per second) technique available at the Advanced Photon Source, USA and Diamond Light Source, UK to investigate the dynamic interactions between the ultrasonic bubbles/acoustic flow and the solidifying phases in a Bi-8%Zn alloy. The experimental results were complimented by numerical modelling. The chaotic bubble implosion and dynamic bubble oscillations were revealed in-situ for the first time in liquid metal and semisolid metal. The fragmentation of the solidifying Zn phases and breaking up of the liquid-solid interface by ultrasonic bubbles and enhanced acoustic flow were clearly demonstrated and agreed very well with the theoretical calculations. The research provides unambiguous experimental evidence and robust theoretical interpretation in elucidating the dominant mechanisms of microstructure fragmentation and refinement in solidification under ultrasound.

1. Introduction

Applying ultrasonic waves in a liquid medium creates an alternating acoustic pressure field [1,2]. When the pressure is above a certain threshold, ultrasonic bubbles and acoustic streaming flow are produced in the liquid. The ultrasonic bubbles vibrate according to the alternating pressure, grow, coalesce and finally collapse, creating local shock waves with high pressure and temperature in the nearby region. This is commonly known as ultrasonic cavitation [3–11]. These are highly dynamic nonlinear phenomena and when they occur in liquid metal, especially during the solidification processes, the heat/mass transfer, fluid flow and ultimately the

microstructures of the solidifying metal are affected [12–18]. Previous investigations on the ultrasonic treatment (UST) of metallic alloys have shown that refined, equiaxed grain structures can be produced, thereby, improving the mechanical properties such as yield strength and fracture toughness [3,12,17,19]. Furthermore, the soundness of castings can also be enhanced by UST due to a reduction in shrinkage, hot tearing, and more uniform distribution of the refined secondary phases and/or reduced micropores [20,21]. However, the exact mechanisms of how ultrasonic bubbles and acoustic flow interact with the solidifying phases, especially the highly dynamic phenomena occurring at the liquid-solid (L-S) interface have not been fully understood. This is mainly due to the opaqueness of liquid metals, which prevents direct real-time observation of the dynamic interactions between the ultrasonic waves, bubbles, acoustic flow at the L-S interface. Previous studies have used water or water-based solutions [7,22], as well as organic

transparent alloys [8,11,23], to mimic liquid metal alloys in order to study the effects of ultrasonic bubbles and streaming flow during solidification under visible light illumination. For example, by using camphene [11], sucrose solutions [7,24], and succinonitrile-1% camphor solution [8], it was found that growing dendrites were fractured by the oscillating bubbles or shock waves generated at bubble implosion. These investigations provide valuable visual data for understanding the effects of UST.

Nevertheless, organic transparent alloys and solutions are different from liquid metal alloys in terms of density, viscosity, surface tension, heat/mass transfer coefficient and sound velocity. For example, the density of succinonitrile-1% camphor (an organic alloy) is 0.97 g/cm^3, less than one third of Al alloys (~2.7 g/cm^3); while the thermal diffusivity (1.16×10^{-7} m^2/s [8]) is 726 times less than pure aluminium (8.418×10^{-5} m^2/s [25]). These differences in physical properties make it inappropriate to simply apply the findings from organic alloy systems to metallic systems. In addition, during metal solidification, the viscosity, surface tension, sound velocity and fraction of the liquid and solid phases are governed predominantly by changes in temperature [26,27]. The resulting ultrasonic bubbles and acoustic flow are also very sensitive to the thermophysical properties of the different media and temperatures. Therefore, it is essential to study in real-time the ultrasonic bubbles and acoustic flow in liquid and solidifying metal to understand fully how ultrasonic bubbles and acoustic flow interact with the liquid metal, the solidifying phases and the L-S interface.

X-rays have been used to "see" and investigate the internal structures of metals and other opaque materials for over a century [6,28—32]. Since the mid-1990s, the development of the 3rd generation synchrotron X-ray facilities around the world has made high brilliance X-rays and the relevant instruments available for materials scientists to study in-situ the dynamics of metal solidification [29—33]. The European Synchrotron Radiation Facility (ESRF) in Grenoble was the first of the 3rd generation hard X-ray sources (6-GeV storage ring) to operate in 1994. The ERSF was followed by the Advanced Photon Source (APS) at Argonne National Laboratory (7 GeV) USA in late 1996, and SPring-8 (8 GeV) in Harima Science Garden City in Hyogo prefecture, west of Osaka, Japan in late 1997 [34]. In the early 21st century, a number of medium energy sources have become operational, including the Diamond Light Source (DLS, 3 GeV), UK in October 2007. Mathiesen et al. [29—31] was among the first to study in-situ the cellular and dendritic growth of Sn-Pb alloys at Beamline ID22 of ESRF. The dynamics of quasi-steady ultrasonic bubbles in a liquid Sn-Bi alloy was first studied by Lee et al. [35] using ultrafast synchrotron X-ray imaging (4526 fps) at the sector 32-ID-B of APS. Ultrasonic bubbles in liquid Al-Cu alloy were studied by Huang et al. [6] at Shanghai Synchrotron Radiation Facility. However, the 2 fps image acquisition rate used in [6] was too low to reveal the dynamic phenomena of ultrasonic bubbles and acoustic flow.

Since 2011, the researchers in Mi's group have carried out extensive studies on the dynamics of ultrasonic bubbles and acoustic flow in liquid metals and their effects on the solidification microstructures using the ultrafast synchrotron X-ray imaging facility (up to 271,554 fps) available at the sector 32-ID-B of APS. The preliminary results were reported in Ref. [36].

In this paper, we further report the very recent results of systematic real-time studies of the interactions between ultrasonic bubbles/acoustic flow and the solidifying phases of a Bi-8 wt%Zn alloy. The focus of the experimental research is to obtain real-time and visual information for ultrasonic processing of metal alloy melt during the solidification process, and to elucidate the fragmentation mechanism of the solidifying phases by bubble implosion and oscillation; and the break-up of the L-S interface by acoustic flow. The Gilmore model [37] was used to calculate the pressure and velocity at the bubble wall. The data and new findings from the experiments and simulation allow us to explain clearly the underlying mechanisms of how solidifying phases were fractured and redistributed in the solidifying melt, which is the most dominant mechanism for structure refinement during the different stages of the solidification process.

2. Experiment

2.1. Alloy, experimental apparatus and setup

A Bi-8 wt% Zn alloy, made by melting high-purity Bi (99.999%) and Zn (99.99%) rods, was chosen as the alloy in this research because of its low melting temperature (liquidus temperature of 341 °C, and solidus temperature of 254.5 °C [36]), and the adequate X-ray absorption contrast between the Bi matrix and the Zn phase. Table 1 lists the alloy properties at 427 °C, the temperature where the bubble implosion were imaged.

Fig. 1 shows a CAD rendering of the experimental setup at the 32-ID-B of APS [36]. The sample holder was made from a quartz tube with a flat thin channel region (15 × 10 × 0.30 mm) in the middle that can be filled with ~300 μm thick liquid metal. The thickness was tested and optimised by previous experiments [36] to obtain sufficient X-ray transmission through the liquid metal and to have enough space for ultrasonic bubbles (generated from the sonotrode tip positioned at ~0.25 mm above the thin channel) to flow through freely. Bi-8% Zn alloy cast rods (Ø9 × 30 mm) were used as the feedstock alloy and melted by using a purposely-made furnace that enclosed the quartz sample holder. A slot (5 mm wide and 30 mm long) was opened in the furnace front and back plates, allowing the X-ray beam to pass onto the thin channel area and projecting the transmitted X-ray onto the scintillator. The dimensions of the sample holder and quartz tube, and the description of the furnace are detailed in [36]. A brass rod (Ø9 × 15 mm) was used as a heat sink at the bottom of the sample holder to generate the required thermal gradient along the z-direction (as described later). Three K-type thermocouples marked as TC1, TC2, and TC3 in Fig. 1 were positioned at the top, middle and bottom of the channel, respectively, to monitor and record the temperatures of the alloy during melting and cooling operations. Both TC1 and TC2 were 250 μm in diameter while TC3 was 500 μm in diameter and the distance between the neighbouring thermocouple was ~4.5 mm.

A Hielscher UP100H ultrasound processor (100 W, 30 kHz), together with a MS2 sonotrode (made of Ti-alloy with a tip diameter of Ø2, 74 mm long) were used to generate ultrasonic waves inside the liquid metal. The ultrasound power was adjustable from 20 W to 100 W with a step of 20 W. The actual vibration amplitudes of the sonotrode tip at the ultrasound powers of 20, 60 and 100 W were measured by using a Phantom™ V7.3 high speed camera, and were used to calculate [3] the corresponding ultrasound intensities as shown in Table 1 (details in Ref. [38]). The ultrasound processor

Table 1
The properties of the Bi-8% Zn alloy, the quartz sample holder, and the ultrasound parameters used in the experiments and the Gilmore model [37].

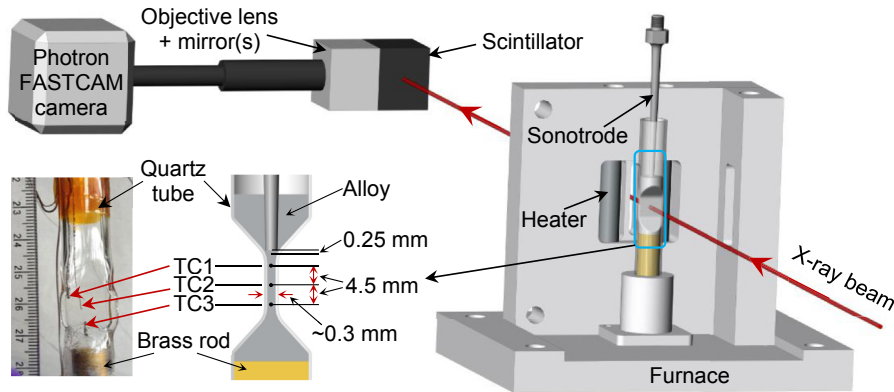| Material	Bi-8% Zn
Density, ρ_0	9561 kg m^{-3}
Viscosity, μ	1.5×10^{-3} Pa s
Surface tension, σ	0.376 N m^{-1}
Sound speed in liquid *Bi-8% Zn*, c_0	1790 m s^{-1}
Sound speed in quartz tube, c*	5300 m s^{-1}
Density of quartz tube, ρ^*	2.23×10^3 kg m^{-3}
Ultrasound frequency, f	30 kHz
Ultrasound power	0, 20, 60, 100 W
Ultrasound intensity	0, 276, 926, 1839 W/mm^2

Fig. 1. A CAD rendering of the experimental setup at the 32-ID-B of APS. A specially-made furnace (the front part was open to show the sample holder) was used for sample heating. A purposely-made quartz tube with a thin channel of 0.3 mm thick (bottom left) was used to contain the liquid metal where X-ray images were taken. The sonotrode tip was positioned 0.25 mm above the thin channel; three K-type thermocouples (TC1, TC2, and TC3) were positioned at the top, middle and bottom of the thin channel to measure the temperatures of the liquid metal during the solidification.

was mounted on a precision linear stage where the height could be adjusted independently to the quartz tube, facilitating X-ray imaging either on the tip of the sonotrode or in the regions of interest within the thin channel. A custom-made relay trigger device was used to precisely control the application of ultrasound into the melt and the synchronisation with the high speed camera for imaging.

2.2. Beamlines and X-ray parameters

The synchrotron X-ray imaging experiments were conducted at Sector 32-ID-B of APS, and Beamline I12 of DLS. Sector 32-ID-B is a dedicated undulator X-ray source designed to fully utilise the 500 ns X-ray pulse by synchronizing the X-ray pulse from the storage ring with the ultrafast shutter and the camera on the beamline, delivering an ultrafast image acquisition rate of up to 271,554 fps with a spatial resolution of 1 μm/pixel in a field of view of 1×1 mm. Synchronisation ensured that images were taken within the 500 ns exposure time, providing an image temporal resolution of ~500 ns regardless of the image acquisition rate. In this study, white beam was used and the undulator gap was set at 18 mm, allowing most of the white beam intensity to be located within the first harmonic around 7.7 keV, with a peak irradiance of 3.4×10^{14} ph/s/mm^2/0.1% bw, and a natural bandwidth of 0.4 keV full-width at half-maximum. In the image sequences reported in this paper, acquisition rates of 135,780 and 5413 fps were used and the image sequences were recorded using a CMOS camera (Photron FASTCAM SA1.1) coupled to a scintillator (LYSO:Ce) with a $10 \times$ optical microscope objective lens and a mirror set at 45°. The sample-to-detector distance was 980 mm.

The Beamline I12 at DLS provides synchrotron X-ray with a peak flux of 10^{12} ph/s/mm^2/0.1%bw and is a dedicated high energy instrument on a 4.2 T wiggler source, offering white or monochromatic X-ray beams in the range 50–150 keV. Filtered white beam was used to produce the highest possible flux without causing damage to the sample and detector. Experiments at DLS used the similar setup as showed in Fig. 1, except that the imaging system was a Vision Research Phantom™ 7.3 high speed camera, coupled to a scintillator via a $1.8 \times$ objective lens and two 90° turning mirrors. Image acquisition rates used were 1000 and 1500 fps with a 700 μm thick Lutetium Aluminium Garnet detector doped with Cerium (LuAG:Ce). The sample-to-detector distance was 900 mm.

At Beamline I12, a view field of 6.6×5.4 mm with a spatial

resolution of 12.2 μm/pixel was adopted as compared to the 1×1 mm with a spatial resolution of 1 μm/pixel at Sector 32-ID-B. The wider field of view on Beamline I12 is therefore suitable for studying the interactions between ultrasonic bubbles/acoustic flow and the L-S interface/semisolid phases; while Sector 32-ID-B provided higher temporal and spatial resolution to better resolve the dynamics of the bubble implosions/oscillations.

2.3. Temperature control during solidification

The desired temperature gradient along the z-direction (Figs. 1 and 2) within the thin channel was controlled by adjusting the z-direction position of the quartz tube relative to the heaters in the furnace and with the use of the brass rod heat sink below the thin channel. By imposing a suitable temperature gradient, a clear liquid-to-solid transition zone was created in the middle of the thin channel, e.g., at the location between TC2 and TC3 as shown later in Fig. 3, allowing the evolution of the L-S interface to be studied in-situ when ultrasonic bubbles and the acoustic flow are present in the view field.

The feedstock alloy was heated up over 450 °C and then held at ~427 °C (TC1) for at least 1500 s to ensure the alloy was fully melted
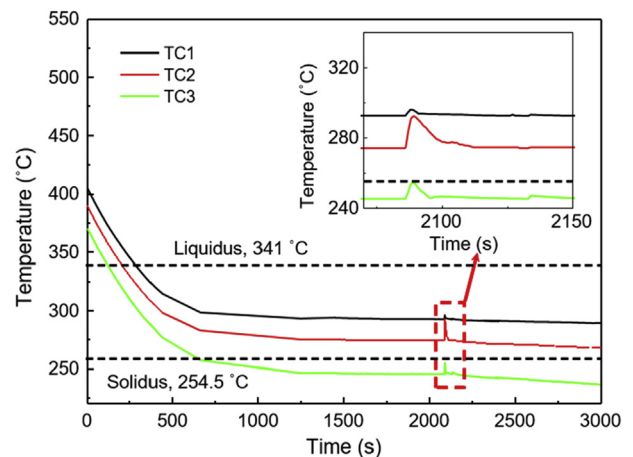

Fig. 2. The temperature profiles recorded during the cooling processes of the Bi-8% Zn alloy. The cooling rate was ~0.2 °C/s. The inset shows the temperature jump when the ultrasound was applied.
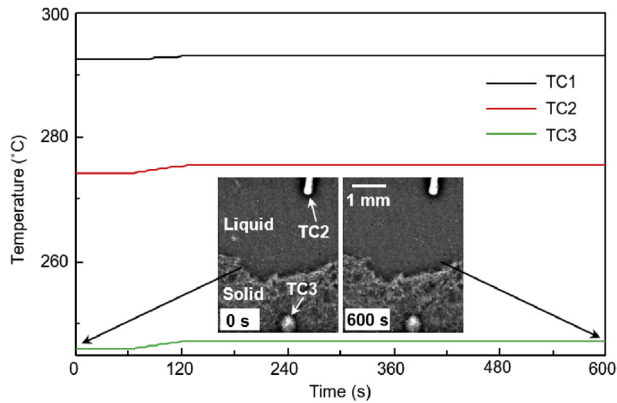
Fig. 3. The temperature profiles recorded during the cooling processes of the Bi-8% Zn alloy. The insets show the X-ray images of the L-S interface before and after continuously exposed to the X-ray beam for 600 s at Beamline I12. The white solid particles are the primary Zn phases.

and completely filled in the thin channel of the sample holder. The liquid metal in the thin channel was then cooled at a rate of ~0.2 °C/s with a temperature gradient of ~5.2 °C/mm between TC1 and TC3. Fig. 2 shows the typical temperature profiles used during the controlled cooling process to form a clear L-S solidification front between TC2 and TC3; the figure inset shows sudden temperature jump in a couple of seconds during image acquisition due to the application of ultrasound. Nevertheless, this relatively small temperature jump during image acquisition gave negligible effects on the solidifying microstructures since the heat was quickly dissipated and the temperature was back to the target temperature.

Owing to the heating effect from the X-ray white beam at the Beamline I12 (0.028 W/mm^2 for Bi-8% Zn) [39], it was noticed that the temperature had a jump of <1 °C at TC2 and TC3 when the X-ray shutter was opened. In order to investigate potential effects on the solidification of alloy, an experiment without ultrasound was conducted under the same cooling rate as in Fig. 2 (~0.2 °C/s). Fig. 3 shows measured temperature profiles with applied white beam, insets are real-time L-S interface images subjected to 0 and 600 s illumination of the white beam. The white solid particles are the primary Zn phase. The two images are identical, indicating that there was no obvious influence from the heating of the white beam. Thus, the beam illumination effect was neglected in this research. To capture the L-S interface, the temperatures at TC2 and TC3 were fixed at ~274 °C and ~245 °C, respectively. The temperature gradient between TC2 and TC3 is ~6.4 °C/mm and this temperature gradient allowed a clear L-S solidification front to be formed between TC2 and TC3.

3. Results and discussion

3.1. Ultrasonic bubble oscillation and implosion

Fig. 4 shows the evolution (the changes of bubble radius with the alternating acoustic pressure) of a single bubble immediately below the sonotrode tip inside the Bi-8% Zn alloy at 427 °C. The ultrasonic intensity applied was 276 W/mm^2 (equivalent to an ultrasound power of 20 W) and the maximum acoustic pressure immediately below the sonotrode tip, i.e. 0.02 mm below, was calculated as 14.5 MPa by using the Helmholtz equation (see Fig. 1 in Ref. [38]). The X-ray images were captured using an acquisition speed of 135,780 fps at the Sector 32-ID-B (the maximum image acquisition rate of 271,554 fps gives too small view field to accommodate sufficient number of bubbles in the view field). A

bubble was seen in Fig. 4a-2 with a radius of ~8 μm and expanded to ~23 μm in Fig. 4a-3 when the sonotrode tip moved up (the rarefaction part of the acoustic cycle). Bubble implosion occurred after the sonotrode started to move down (the compression part of the acoustic cycle), resulting in a blurred-and-misty circular region (Fig. 4a-5) with the release of high pressure shock wave to the surrounding liquid [36]. The imploded bubble produced many tiny bubbles or bubble fragments. Those with the size of <1 μm are too small to be seen in Fig. 4a-6 due to the spatial resolution limit of the X-ray imaging technique. However, Tan [39] has reported in his PhD thesis (in Chapter 4) many cases in water (when 271,554 fps was used) where bubble fragments of a few micrometres were observed after bubble implosion. These bubble residuals or fragments acted as nuclei for the next cycle of bubble nucleation, expansion and implosion. Many similar observations and recordings were made during the ultrafast synchrotron X-ray imaging experiments at APS. These evidences clearly indicate that, in the region below and near the sonotrode tip where acoustic pressure is sufficiently high, the whole life cycle of bubble nucleation, expansion and implosion can be completed in just one ultrasound period, i.e. 33.3 μs in this case. The bubble fragments created at bubble implosion is the overwhelming resource of the bubble nuclei for the next ultrasound period. Each implosion creates many more bubble nuclei for the next period. Such multiplication effect or chain-reaction nature are the dominant phenomenon at the region near the sonotrode tip. When the region was fully developed, an ultrasound cavitation zone was created in the liquid in which many different size bubbles oscillated very quickly and energetically, accompanied by many instances of chaotic and violent implosions of some bubbles when their diameters reach the critical threshold in the alternating acoustic pressure field. Moving downward from the sonotrode tip surface, the acoustic pressure in the liquid metal attenuates exponentially [40], and the dynamic behaviours of ultrasonic bubbles changed accordingly as discussed below.

3.2. Detachment of the solid phases from the L-S interface by oscillating bubbles and acoustic flow

Fig. 5a is a sequence of X-ray images captured at Beamline I12 using 1500 fps, showing the cyclic impact and pounding of one oscillating bubble at the L-S interface in the Bi-8% Zn alloy. The images were taken ~5.5 mm below the sonotrode with an ultrasound intensity of 926 W/mm^2. It is clearly demonstrated that the bubble was pulsating cyclically at the L-S interface, pounding and knocking off the primary Zn particles, and gradually eroding into the solid phase. Fig. 5b and c shows the pressure and velocity profiles at the bubble wall calculated by the Gilmore model based on the bubble conditions in Fig. 5a. In addition to the pressure profiles in the steady state oscillating condition, the pressure profiles of the bubble in subharmonic oscillations were also included as highlighted in Fig. 5b, where the peak pressure values varied [41]. Fig. 5b shows that the maximum bubble wall pressure is ~20 MPa with the maximum velocity of ~20 m/s. While the mean pressure and velocity are 7.5 MPa and 12.5 m/s, respectively.

These are significant periodic pressure and momentum conditions imposed on the surrounding liquid or solid phases (if there are any) in the viscous melt. The detached Zn particles survived and moved upwards by the ultrasound-enhanced acoustic flow back into the bulk liquid. Clearly, the erosion of the L-S interface is due to the combined effects of cyclic pounding of the bubble and flush of the acoustic flow onto the L-S interface.

To quantify and differentiate the contributions on the detachment of the solid phases from the L-S interface by the ultrasonic bubble and acoustic flow, Fig. 5d plots the increase in area of the liquid phase (E_a) and the bubble depth (E_d) as function of time in
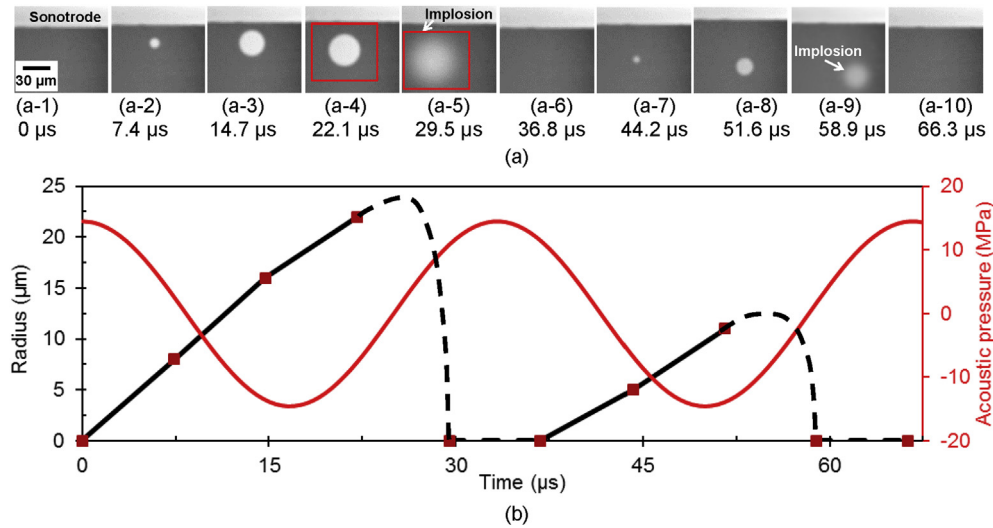
Fig. 4. (a) An X-ray image sequence acquired using 135,780 fps at Sector 32-ID-B of APS, showing the bubble implosion immediately below the sonotrode tip in the Bi-8% Zn alloy at 427 °C; the input ultrasonic intensity was 276 W/mm² (an ultrasound power of 20 W). (b) The bubble radius measured from the images in (a), and their correlation with the acoustic pressure applied into the liquid metal. The dashed lines indicate the sudden drop of bubble radius at the instance of bubble implosion.

the view field by using the L-S interface in Fig. 5a as the reference. It is interesting to see that both E_a and E_d increased linearly with time, and the rate of erosion can be determined from the slopes of the two linear regression fitting lines. They are 0.44 mm²/s and 0.20 mm/s for E_a and E_d, respectively. Apparently, the oscillating bubble is leading the erosion and phase detachment at the L-S interface.

3.3. Fragmentation of a Zn phase by oscillating bubbles

To further investigate the interactions of oscillating bubbles with the surrounding solidifying phases during ultrasound treatment (UST), we designed a special bubble trap and inserted it inside the thin channel area of the quartz sample holder as shown in Fig. 6a. It was made of a polished Al-20% Cu thin plate of ~250 μm thick with slots of different widths and depths separated by the 'fingers' of 250 μm wide. The slots were machined by electrical discharge machining and used for trapping the ultrasonic bubbles at different distances below the sonotrode tip (Fig. 6a). This arrangement allowed us to be able to nucleate and grow solid phases (Zn phases in this case and the primary Zn phases in a Bi-8% Zn alloy grew into needle-shaped phases [38]) from the tip of the 'fingers' (because it is a chilled and solid base in the solidification temperature range of the Bi-8% Zn alloy); and also to have higher probability to capture the incoming ultrasonic bubbles at the 'fingers' tip region. Using such arrangement, we were able to successfully capture the pulsating of a single ultrasonic bubble at a growing needle-shaped Zn phase as demonstrated in Fig. 6b-1 to b-6. In the experiment, the sonotrode tip was located 5 mm above the tip of the 'finger', and a single needle-shaped Zn phase of ~200 μm long (Fig. 6b-1) was observed to grow from the tip of the 'finger' in the view field. When an ultrasound of 926 W/mm² was applied from above, a single bubble, together with the acoustic flow, was observed to move down and reach at the L-S interface, pulsating on the right-hand side of the long Zn phase (Fig. 6b-2). The bubble kept pulsating on the tip of the Zn phase (Fig. 6b-3 and b-4) and finally passed through the Zn phase at 113.3 ms as showed in Fig. 6b-5. From the instant when the bubble landed onto the Zn phase (3.3 ms in Fig. 6b-2) to the moment it passed the Zn phase (113.3 ms in Fig. 6b-5), the bubble was seen pulsating energetically and cyclically on top of the long Zn phase for 110 ms, equivalent to ~3330

ultrasound wave period. After an extra ~14.7 ms, the long Zn solid particle was seen clearly fractured and the fragment was washed away together with the bubble by the acoustic flow, leaving a ~60 μm long residual part still embedded in the solid phase below the L-S interface (Fig. 6b-6).

To further elucidate the fragmentation mechanism of the Zn phase, we again used the Gilmore model to calculate the pressure and velocity profiles at the bubble wall for this specific bubble showed in Fig. 6b, and the results are shown in Fig. 6c. The maximum bubble wall pressure (the pressure amplitude) was ~40 MPa. By excluding the low pressures (the small pressure values in each wave period) from the subharmonic oscillation behaviour [41], the majority of the pressure amplitude due to bubble oscillation was in the range of 20–30 MPa (Fig. 6c-1). While the maximum velocity (velocity amplitude) was calculated as ~±30 m/s as shown in Fig. 6c-2.

To understand more quantitatively whether such cyclic pressure and momentum are the dominant cause for fracturing the Zn phase or not, we calculated the fatigue strength and fatigue life of the Zn phase at 270 °C. Because of the lack of fatigue strength data for pure zinc in the open literature, we used the very rich experimental data found for a commercial Zn-4% Al alloy for the analyses. Generally, the fatigue strength and fatigue life of alloys can be calculated by Basquin's Law [42]:

$$N = CS^{-k} \tag{1}$$

where, S is the cyclic stress amplitude; N is the number of cycles to failure; C and k are material constants at a given temperature. Applying logarithm operation on both sides, we obtain:

$$\log N = \log C - k \log S \tag{2}$$

Thus, (log N) versus (log S) follows a linear relationship with constant k as the slope and an interception at log C. Sawalha [43] investigated the fatigue behaviour of a Zn-4% Al alloy at 20, 50 and 100 °C. The measured fatigue experimental data were used to determine the material constants at each temperature. As the low-cycle fatigue mechanism is different from that of the high-cycle fatigue [44], three data points below 90 MPa, i.e. high-cycle fatigue with $N > 10^5$ cycles in Ref. [43] were selected at each
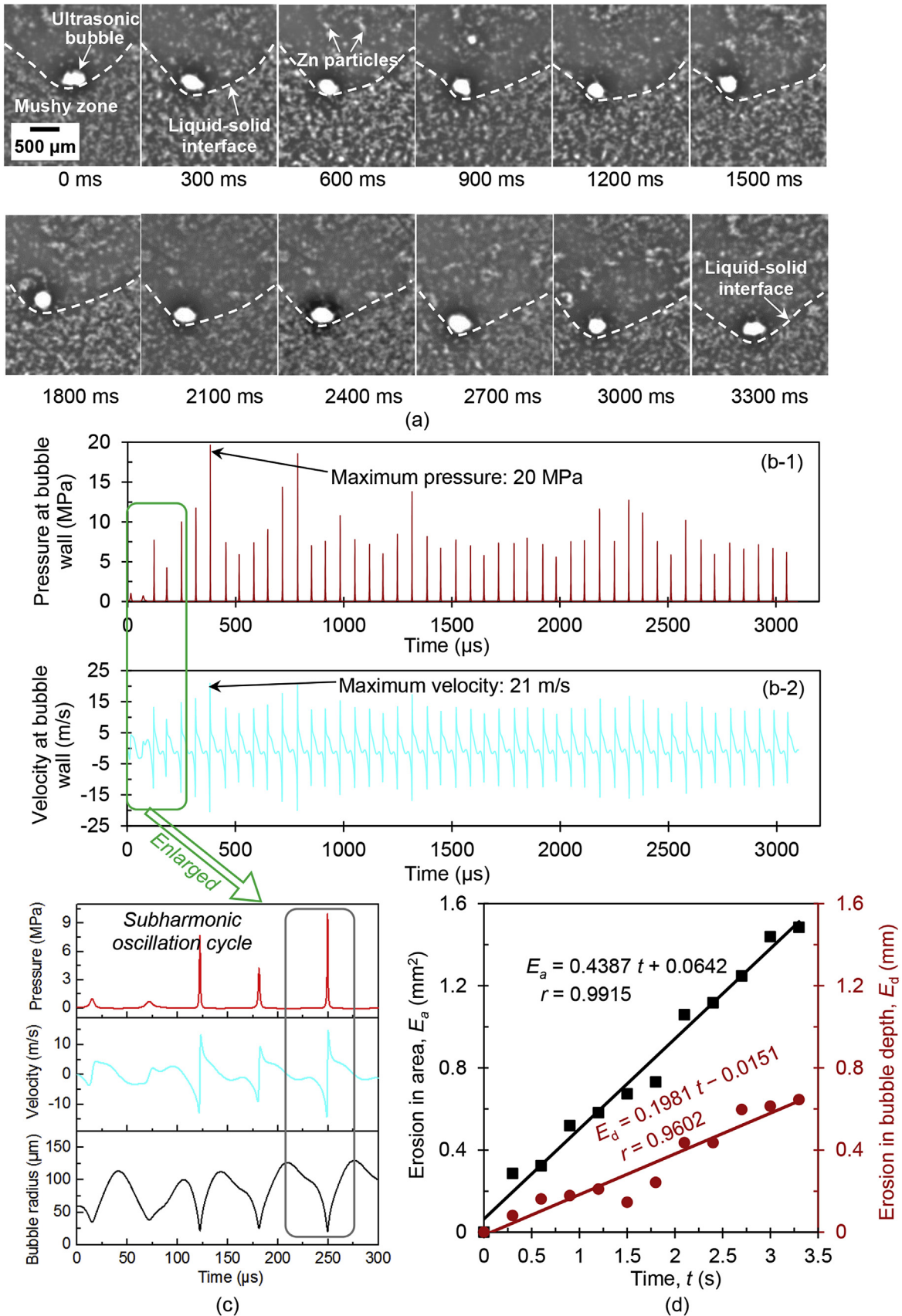
Fig. 5. (a) A sequence of X-ray images, showing the cyclic impact and pounding of the oscillating bubble at the L-S interface in the Bi-8% Zn alloy; (b) the pressure and velocity profiles at bubble wall calculated using the Gilmore model (initial bubble radius = 60 μm, maximum acoustic pressure amplitude = 0.24 MPa) corresponding to the bubble conditions in (a); (c) an enlarged section for the framed area in (b); (d) the erosion of the L-S interface as a function of time, solid lines are the fitted linear regressions. The temperature before UST at TC2 was 274 °C, and 245 °C at TC3; the view field centre was ~5.5 mm below the sonotrode tip, and the ultrasound intensity applied was 926 W/mm² (a power of 60 W).

temperature to fit into Eq. (2) (see Fig. 3 in Ref. [38]). The fitted curves are showed in Fig. 7a and b, corresponding data are shown in Table 2. Clearly, both log *C* and *k* exhibit a power law relationship with temperature. Hence, log *C* and *k* at 270 °C was determined as 5.11 and 1.10, respectively, by extrapolating the fitting curves in Fig. 7a and b over 270 °C.

Using the material constants in Table 2, the *S-N* curves for the Zn-4%Al alloy at different temperatures were calculated using Eq. (1) and shown in Fig. 7c. The fatigue lives of the Zn-4% Al at 270 °C in the stress level of 20–30 MPa were between 4737 and 3027 fatigue cycles; and at ~25 MPa, the fatigue life was 3700 cycles as highlighted in Fig. 7c. While, Fig. 6b-6 shows clearly that the Zn phase was completely broken after 124 ms, equivalent to 3720 ultrasound wave periods. Furthermore, Fig. 6c-1 shows that the pressure amplitude caused by the oscillating bubbles is mainly in the range of 20–30 MPa. Such an excellent agreement between the experimental observation of the fragmentation of Zn phase in this research and the theoretical analyses for the fatigue lives of the Zn-4% Al alloy (the closest alloy in composition to pure Zn with reported high temperature fatigue data) indicates that the fatigue effect from the oscillating bubble is the dominant factor in breaking the Zn phase. Similar fatigue-type fragmentation of primary intermetallic phases in Al alloys under ultrasound processing in water has been recently reported by Wang et al. [45]. Of course, the momentum of the acoustic flow also plays a minor role in this case as more evidence presented in the next section for the erosion effect from the acoustic flow.

3.4. Break-up of the L-S interface by acoustic flow

To further investigate the effect of acoustic flow on the L-S interface, systematic experiments and image sequences were taken at a deeper area in the thin channel where ultrasonic bubbles were hardly seen in the experiments. Fig. 8 shows the evolutions of the L-S interface under different ultrasound intensities for 2 s for each case. The arrows show the direction of acoustic flow, obtained by tracking the trajectory of the Zn phases flowed with the acoustic flow in the bulk liquid. The fluid flow pattern was found relatively symmetric to the centre of the sonotrode, clockwise on the left and anti-clockwise on the right. Fig. 3 already shows that, without ultrasound (0 W/mm^2), no detachment of solid Zn phase was found at the L-S interface. Fig. 8a indicates that, when an ultrasound of 276 W/mm^2 was applied for 2 s, a very weak acoustic flow was observed, and the L-S interface region remained almost unchanged in 2 s, with just a few 'loose' particles on the L-S interface (marked by white circle) were detached and washed away by the flow. When the intensity was increased to 926 W/mm^2 in Fig. 8b, a strong acoustic flow was observed, causing a 'cleavage' into the solid phase at 150 ms. Then a big piece of the solid Zn phase was broken up and gradually washed away after 280 ms by the flow. The initial relatively flat L-S interface changed significantly, as indicated by the dashed lines. When 1839 W/mm^2 was used, Fig. 8c shows that the L-S interface was quickly broken up by the very strong swirling flow, and completely disappeared from the view field in 1286 ms. It is also important to note that in all cases, the detached solid particles were observed to flow back to the hotter liquid region, carried by the acoustic flow, and survived for a substantial period of time.

The percentage of the detached solid phases in the view field showed in Fig. 8a-c were analysed using a self-coded script in Matlab (see Appendix A in Ref. [38]) and plotted as function of time as shown in Fig. 8d. In addition, the velocities of Zn particles moving were calculated from the travel distance between two adjacent images. Note that particle velocity may underestimate the speed of the liquid acoustic flow due to gravity inertia. Fig. 8e

shows the final percentages of the detached solid phases (after 2 s of UST), and the maximum velocity of Zn particles in the acoustic flow. Using 276 W/mm^2, the maximum particle velocity was <0.2 m/s causing just a few detachment of Zn particles from the interface (<2%). While with 926 W/mm^2, the maximum particle velocity was ~0.65 m/s, and there was a rapid period of particles detachment from 0 to 50 ms, then the erosion slowed down and stabilised after 500 ms, ~25% of the viewed solid phases were eroded away in 2 s. When the intensity was increased to 1839 W/mm^2, the maximum particle velocity reached ~0.95 m/s, and over 80% of the solid phases in the view field were eroded away in 250 ms. The L-S interface was completely destroyed and disappeared after 1286 ms. It needs to be emphasised that the actual velocity of the acoustic flow for each case should be slightly higher than the particle velocity measured. In addition, the velocities of the acoustic flows observed in the semi-solid state in this research are generally higher than those reported in water [46] and organic transparent alloys [2]. The reason is that the alloy used, i.e. Bi-8% Zn, has much higher density and velocity of sound than those of water and organic transparent alloys. Hence more ultrasound energy was generated in the Bi-8% Zn with the same ultrasound input power to produce higher velocity of particle and acoustic flow.

3.5. The dominant mechanisms for microstructure fragmentation and refinement

We analysed hundreds of the real-time X-ray image sequences obtained from APS and DLS at different locations below the sonotrode tip with different ultrasound intensities applied. In summary, in the semi-solid metal melt, (Bi-8% Zn alloy in this research), the application of an ultrasonic wave can produce a chaotic cavitation zone and enhanced acoustic flow. In the region near the sonotrode, higher acoustic pressure produces a cavitation zone within which ultrasonic bubbles oscillate in phase with the alternating acoustic pressure field and move very quickly at the speed of 1–2 m/s. Chaotic bubble implosions are the dominant phenomena in the cavitation zone. The typical example is the case showed in Fig. 4a where a single bubble imploded in just one ultrasound cycle. In this region, the imploded bubbles and the high speed acoustic flow are very efficient in breaking up the solidifying phases and the L-S interface. More importantly, the imploded bubbles generate many bubble fragments which act as bubble nuclei for the next cycle of bubble evolutions.

Moving away from the sonotrode tip, the ultrasound intensity attenuates exponentially, ultrasonic bubbles may not implode instantly, but survive many tens or even thousands of ultrasound cycles and reach a quasi-steady state condition. In this region, the cyclic fatigue effect caused by the oscillating bubbles and the momentum of the acoustic flow (normally with a speed in the range of 0.5–0.6 m/s as showed in Fig. 8e) are the dominant mechanisms in fragmenting the solidifying phases and breaking up the bulk solid phases at the liquid-solid interface into smaller parts. Of course, the effectiveness of such fragmentation is also dependent on the ultrasound intensity as illustrated in Fig. 8d. In addition, the acoustic enhanced flow has another beneficial effect in flowing or redistributing the fragmented solid phases back into the bulk liquid or semi-solid melts. These surviving solid fragments act as new nuclei or small size grains in the subsequent solidification process. Apparently, for many commercial metal alloy systems, such fragmented solid phases or grains that survive and circulate in the semi-solid melt may act very efficiently as embryonic or small-size grains for the subsequent solidification process, promoting very effectively the structure refinement and chemistry homogeneity of the solidified alloys.
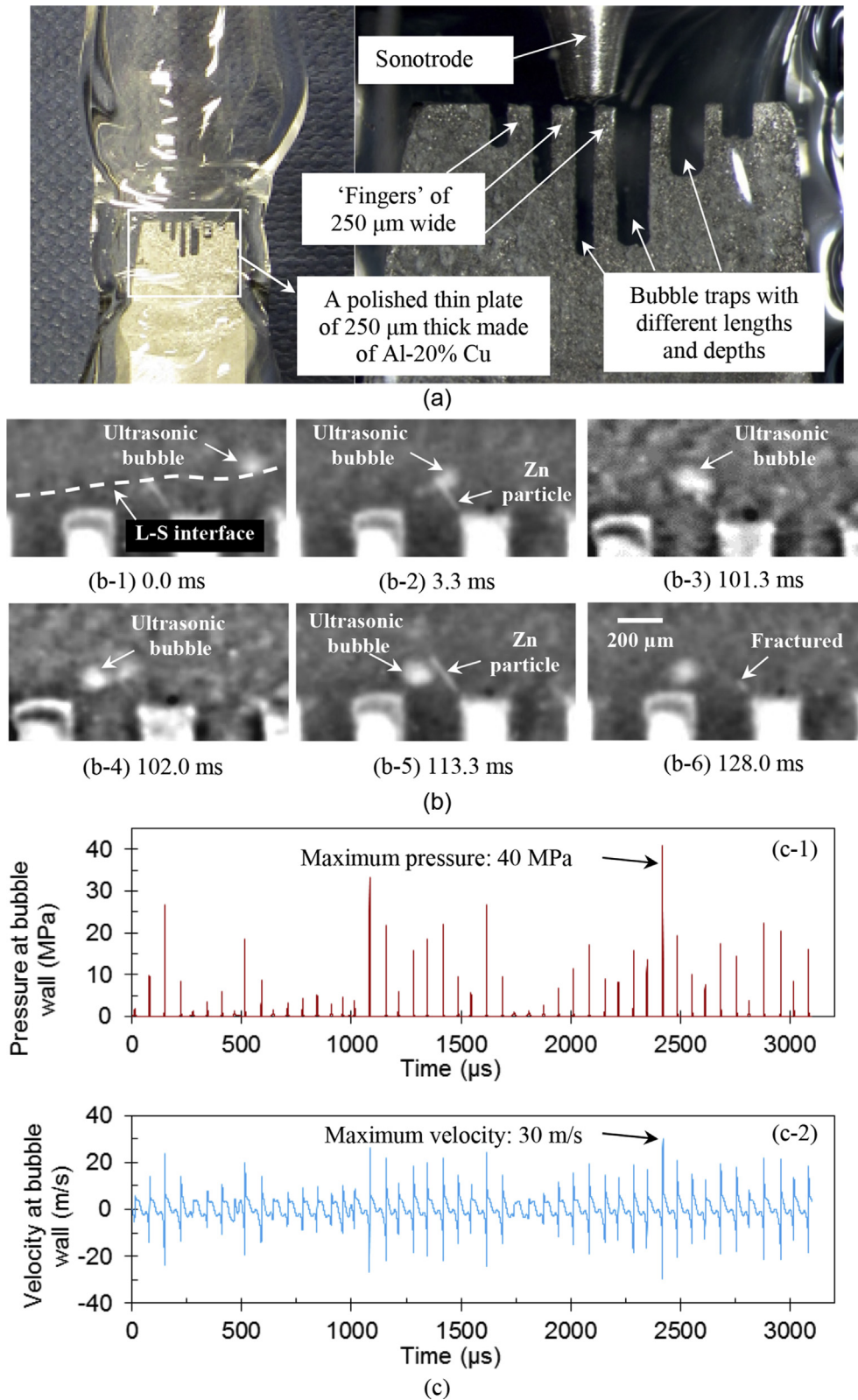
(a)

(b-1) 0.0 ms   (b-2) 3.3 ms   (b-3) 101.3 ms

(b-4) 102.0 ms   (b-5) 113.3 ms   (b-6) 128.0 ms

(b)

(c)

Fig. 6. (a) The arrangement of a bubble trap and the sonotrode tip position in the quartz tube; (b) the fragmentation of a needle-shaped Zn particle by a pulsating ultrasonic bubble; (c) the pressure (c-1) and velocity (c-2) at bubble wall calculated using the Gilmore model (initial bubble radius = 60 μm, maximum acoustic pressure amplitude = 0.33 MPa). Temperature at the bubble position was ~270 °C; the sonotrode tip was located 5 mm above the image centre, with 926 W/mm² UST (a power of 60 W) during the experiment.
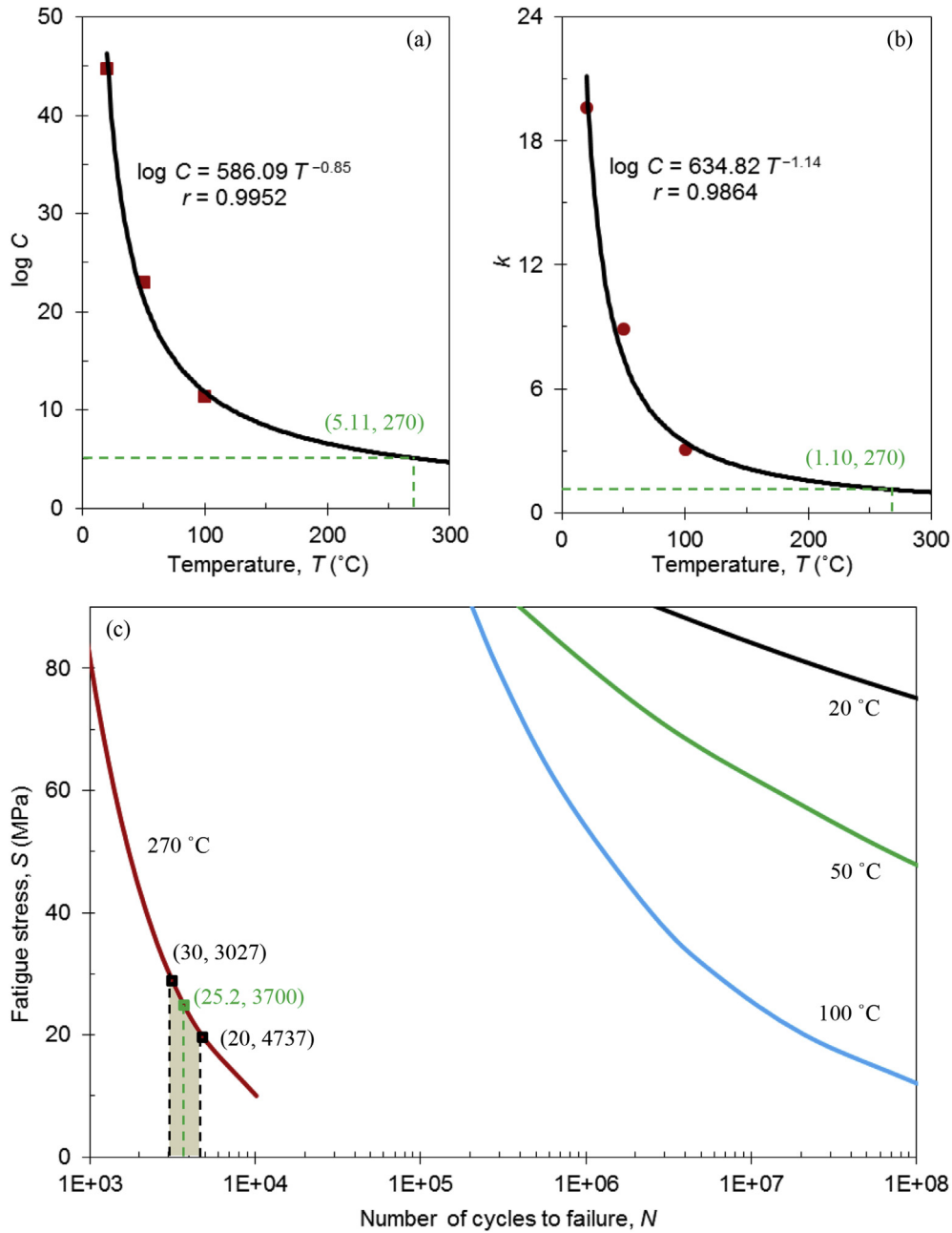
Fig. 7. Plot of material constants (a) log *C* and (b) *k* versus temperature based on Table 2, solid lines are from power law regression; (c) the *N-S* relationships of Zn-4% Al alloy under various temperature, produced by fitting the material constant values in (a) and (b) to Eq. (1).

Table 2
Material constants determined at different temperatures using Eq. (2).

Temperature (°C)	log *C*	*k*
20	44.79	19.62
50	23.00	8.92
100	11.33	3.08
270	5.11	1.10

4. Conclusions

We used the specialty ultrafast synchrotron X-ray imaging facilities available at APS and DLS, and a purposely-made ultrasound solidification apparatus to study in-situ systematically the underlying physics of metal solidification under ultrasonic waves with a focus on the semisolid state. We analysed hundreds of X-ray image video sequences acquired at the carefully controlled solidification conditions with different ultrasound intensities applied. The important findings of this research are:

(i) For the first time, the chaotic implosion and dynamic oscillation of ultrasonic bubbles in liquid and semisolid state of a Bi-8%Zn alloy were revealed in situ. The bubble implosion and oscillation are governed by the ultrasound pressure amplitude. At pressure amplitude of ~14.5 MPa, bubble implosion was observed to occur in one ultrasound period after nucleation and growth. While at ~0.33 MPa, bubble
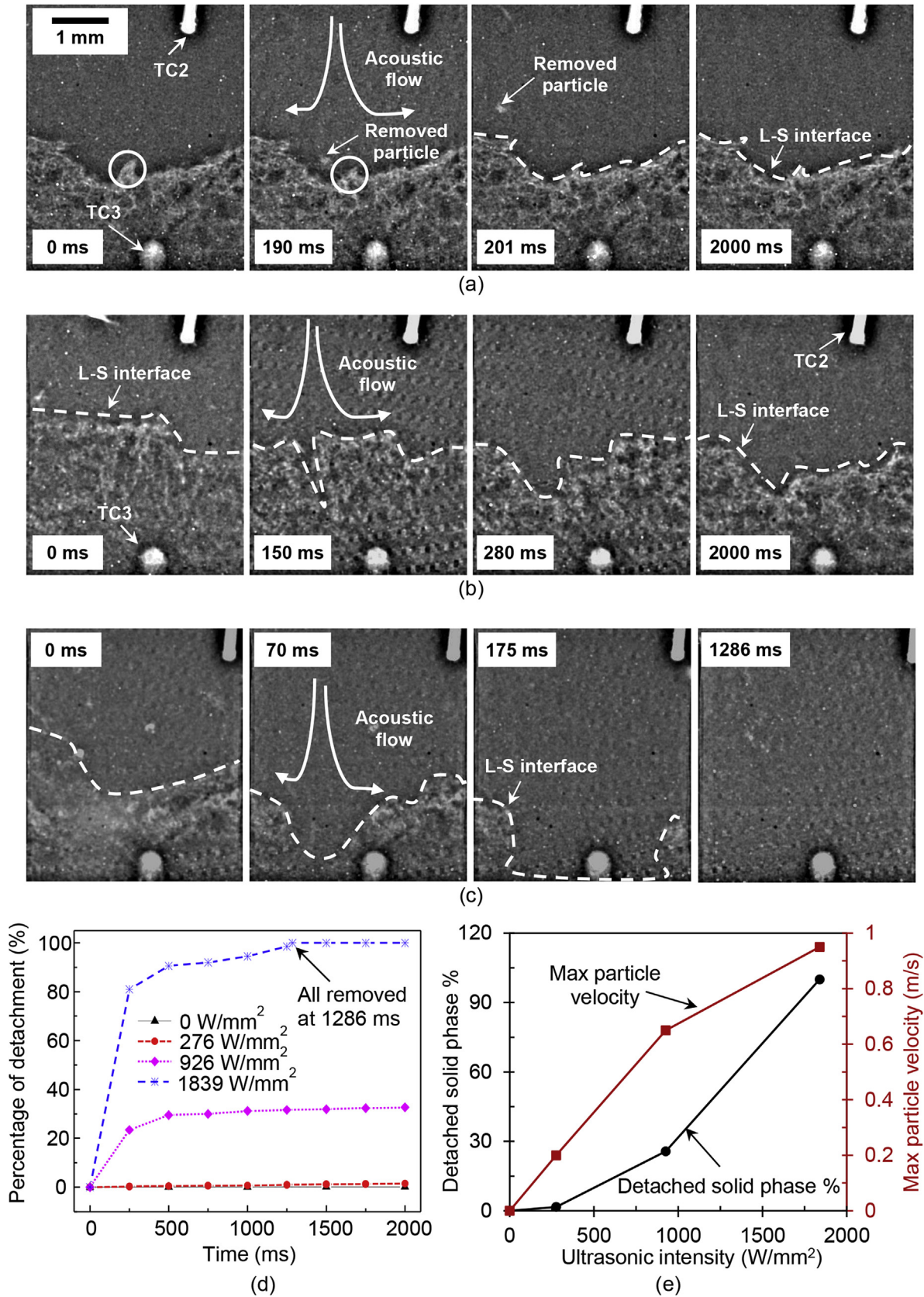
Fig. 8. Image sequences of the L-S interface in semi-liquid Bi-8% Zn alloy, showing the effects from different input ultrasonic intensity (a) 276 W/mm^2, (b) 926 W/mm^2, and (c) 1839 W/mm^2; (d) percentage of the detachments as a function of ultrasonic processing time; (e) final percentage of the detached solid phase (after 2 s of UST) and the maximum velocity of solid particles in the view field versus ultrasonic intensity. Temperature before applying the UST at TC2 and TC3 were 274 °C and 245 °C, respectively. White arrows indicate the direction of ultrasound-induced streaming flow and movement of the Zn phases in the liquid-metal; centre of images was ~6.5 mm beneath the sonotrode tip.

oscillation reach a quasi-steady state that last for many thousands of ultrasonic cycles.

(ii) In the well developed ultrasound cavitation zone, chaotic bubble movement and violent bubble implosion are the dominant phenomena. The imploded bubbles and the high speed acoustic flow are very efficient in breaking up the solidifying phases and the liquid-solid interface.

(iii) In the region where the ultrasonic bubbles reach a quasi-steady state oscillations, the cyclic fatigue effect caused by the oscillating bubbles together with the medium acoustic flow (in the range of 0.5–0.6 m/s) are sufficient in breaking up the solidifying particles and the L-S interface. The fatigue fracture of the Zn phase due to the oscillating bubbles observed from the experiments agreed very well with the theoretical calculation.

Acknowledgements

Appendix A. Supplementary data

Supplementary data related to this article can be found at https://doi.org/10.1016/j.actamat.2017.10.067.

References

[1] B.E. Noltingk, E.A. Neppiras, Cavitation produced by ultrasonics, Proc. Phys. Soc. B 63 (1950) 674–685.

[2] O.V. Abramov, Ultrasound in Liquid and Solid State, CRC Press, London, 1994.

[3] G.I. Eskin, D.G. Eskin, Ultrasonic Treatment of Light Alloy Melts, second ed., CRC Press, Boca Raton, 2015.

[4] W. Lauterborn, C.D. Ohl, Cavitation bubble dynamics, Ultrason. Sonochem 4 (1997) 65–75.

[5] V.B. Kumar, A. Gedanken, G. Kimmel, Z.E. Porat, Ultrasonic cavitation of molten gallium: formation of micro-and nano-spheres, Ultrason. Sonochem 21 (2014) 1166–1173.

[6] H. Huang, D. Shu, Y. Fu, J. Wang, B. Sun, Synchrotron radiation X-ray imaging of cavitation bubbles in Al-Cu alloy melt, Ultrason. Sonochem 21 (2014) 1275–1278.

[7] R. Chow, R. Blindt, R. Chivers, M. Povey, A study on the primary and secondary nucleation of ice by power ultrasound, Ultrasonics 43 (2005) 227–230.

[8] D. Shu, B. Sun, J. Mi, P.S. Grant, A high-speed imaging and modeling study of dendrite fragmentation caused by ultrasonic cavitation, Metall. Mater. Trans. A 43 (2012) 3755–3766.

[9] M. Qian, A. Ramirez, An approach to assessing ultrasonic attenuation in molten magnesium alloys, J. Appl. Phys. 105 (2009) 1–6.

[10] J. Hunt, K. Jackson, Nucleation of solid in an undercooled liquid by cavitation, J. Appl. Phys. 37 (1996) 254–257.

[11] G.M. Swallowe, J.E. Field, C.S. Rees, A. Duckworth, A photographic study of the effect of ultrasound on solidification, Acta Metall. 37 (1989) 961–967.

[12] T.V. Atamanenko, D.G. Eskin, L. Zhang, L. Katgerman, Criteria of grain refinement induced by ultrasonic melt treatment of aluminum alloys containing Zr and Ti, Metall. Mater. Trans. A 41 (2010) 2056–2066.

[13] X. Jian, T.T. Meek, Q. Han, Refinement of eutectic silicon phase of aluminum A356 alloy using high-intensity ultrasonic vibration, Scr. Mater 54 (2006) 893–896.

[14] H. Li, Y. Ni, J. Hong, Ultrasound-assisted preparation, characterization and properties of flower-like ZnO microstructures, Scr. Mater 60 (2009) 524–527.

[15] G.I. Eskin, D.G. Eskin, Production of natural and synthesized aluminum-based composite materials with the aid of ultrasonic (cavitation) treatment of the melt, Ultrason. Sonochem 10 (2003) 297–301.

[16] J.D. Hunt, K.A. Jackson, Nucleation of solid in an undercooled liquid by cavitation, J. Appl. Phys. 37 (1966) 254–257.

[17] L. Zhang, D.G. Eskin, L. Katgerman, Influence of ultrasonic melt treatment on the formation of primary intermetallics and related grain refinement in aluminum alloys, J. Mater. Sci. 46 (2011) 5252–5259.

[18] D. Gao, Z. Li, Q. Han, Q. Zhai, Effect of ultrasonic power on microstructure and mechanical properties of AZ91 alloy, Mat. Sci. Eng. A-Struct 502 (2009) 2–5.

[19] G.I. Eskin, Broad prospects for commercial application of the ultrasonic (cavitation) melt treatment of light alloys, Ultrason. Sonochem 8 (2001) 319–325.

[20] X. Jian, H. Xu, T.T. Meek, Q. Han, Effect of power ultrasound on solidification of aluminum A356 alloy, Mater. Lett. 59 (2005) 190–193.

[21] H. Xu, X. Jian, T.T. Meek, Q. Han, Degassing of molten aluminum A356 alloy using ultrasonic vibration, Mater. Lett. 58 (2004) 3669–3673.

[22] W. Lauterborn, T. Kurz, Physics of bubble oscillations, Rep. Prog. Phys. 73 (2010) 1–88.

[23] J. Pilling, A. Hellawell, Mechanical deformation of dendrites by fluid flow, Metall. Mater. Trans. A 27 (1996) 229–232.

[24] R. Chow, R. Blindt, A. Kamp, P. Grocutt, R. Chivers, The microscopic visualisation of the sonocrystallisation of ice using a novel ultrasonic cold stage, Ultrason. Sonochem 11 (2004) 245–250.

[25] C.P. Kothandaraman, S. Subramanyan, Heat and Mass Transfer Data Book, fifth ed., New Age International, New Delhi, 2004.

[26] L.C. Prasad, R.K. Jha, Surface tension and viscosity of Sn-based binary liquid alloys, Phys. Status Solidi A 202 (2005) 2709–2719.

[27] B.J. Keene, Review of data for the surface tension of pure metals, Int. Mater. Rev. 38 (1993) 157–192.

[28] E.C. Bain, The application of X-ray crystal analysis to metallurgy, Ind. Eng. Chem. 16 (1924) 692–698.

[29] R.H. Mathiesen, L. Arnberg, F. Mo, T. Weitkamp, A. Snigirev, Time resolved X-ray imaging of dendritic growth in binary alloys, Phys. Rev. Lett. 83 (1999) 5062–5065.

[30] R.H. Mathiesen, L. Arnberg, X-ray radiography observations of columnar dendritic growth and constitutional undercooling in an Al-30wt%Cu alloy, Acta Mater 53 (2005) 947–956.

[31] D. Ruvalcaba, R.H. Mathiesen, D.G. Eskin, L. Arnberg, L. Katgerman, In situ observations of dendritic fragmentation due to local solute-enrichment during directional solidification of an aluminum alloy, Acta Mater 55 (2007) 4287–4292.

[32] W.U. Mirihanage, K.V. Falch, I. Snigireva, A. Snigirev, Y.J. Li, L. Arnberg, Retrieval of three-dimensional spatial information from fast in situ two-dimensional synchrotron radiography of solidification microstructure evolution, Acta Mater 81 (2014) 241–247.

[33] B. Cai, S. Karagadde, L. Yuan, T.J. Marrow, T. Connolley, P.D. Lee, In situ synchrotron tomographic quantification of granular and intragranular deformation during semi-solid compression of an equiaxed dendritic Al-Cu alloy, Acta Mater 76 (2014) 371–380.

[34] A. Saegusa, World's biggest synchrotron open for business, Nature 389 (1997), 653–653.

[35] T.L. Lee, J.C. Khong, K. Fezzaa, J. Mi, Ultrafast x-ray imaging and modelling of ultrasonic cavitations in liquid metal, Mater. Sci. Forum 765 (2013) 190–194.

[36] D. Tan, T.L. Lee, J.C. Khong, T. Connolley, K. Fezzaa, J. Mi, High-speed synchrotron X-ray imaging studies of the ultrasound shockwave and enhanced flow during metal solidification processes, Metall. Mater. Trans. A 46 (2015) 2851–2861.

[37] J. Mi, D. Tan, T.L. Lee, In situ synchrotron X-ray study of ultrasound cavitation and its effect on solidification microstructures, Metall. Mater. Trans. B 46 (2015) 1615–1619.

[38] B. Wang, D. Tan, T.L. Lee, J.C. Khong, F. Wang, D. Eskin, T. Connolley, K. Fezzaa, J. Mi, Data and videos for ultrafast synchrotron X-ray imaging studies of metal solidification under ultrasound, Data Brief (2017) (submitted for publication, in this issue).

[39] D. Tan, In Situ Ultrafast Synchrotron X-ray Imaging Studies of the Dynamics of Ultrasonic Bubbles in Liquids, PhD Thesis, University of Hull, United Kingdom, 2015.

[40] S. Majumdar, P.S. Kumar, A. Pandit, Effect of liquid-phase properties on ultrasound intensity and cavitational activity, Ultrason. Sonochem 5 (1998) 113–118.

[41] W. Lauterborn, Numerical investigation of nonlinear oscillations of gas bubbles in liquids, J. Acoust. Soc. Am. 59 (1976) 283–293.

[42] S. Nagarjuna, M. Srinivas, K. Balasubramanian, D.S. Sarmat, Effect of alloying content on high cycle fatigue behaviour of Cu-Ti alloys, Int. J. Fatigue 19 (1997) 51–57.

[43] K. Sawalha, The Fatigue Properties of Pressure Diecast Zinc-aluminium Based Alloys, PhD Thesis, Aston University, United Kingdom, 1991.

[44] F.C. Campbell, Elements of Metallurgy and Engineering Alloys, ASM International, Ohio, 2008.

[45] F. Wang, I. Tzanakis, D.G. Eskin, J. Mi, T. Connolley, In-situ observation of ultrasonic cavitation-induced fragmentation of the primary crystals formed in Al alloys, Ultrason. Sonochem 39 (2017) 66–76.

[46] M.C. Schenker, M.J.B.M. Pourquié, D.G. Eskin, B.J. Boersma, PIV quantification of the flow induced by an ultrasonic horn and numerical modeling of the flow and related processing times, Ultrason. Sonochem 20 (2013) 502–509.